

Research Article

Parametric Study on the Ground Control Effects of Rock Bolt Parameters under Dynamic and Static Coupling Loads

Zequan Sun,¹ Lishuai Jiang ,^{1,2} Jinqun Jiang,¹ Xingyu Wu ,¹ Naser Golsanami,¹ Wanpeng Huang,¹ Peipeng Zhang,¹ Zhongtao Niu,³ and Xiaoyi He⁴

¹State Key Laboratory of Mining Disaster Prevention and Control, Shandong University of Science and Technology, Qingdao 266590, China

²Shandong Key Laboratory of Civil Engineering Disaster Prevention and Mitigation, Shandong University of Science and Technology, Qingdao 266590, China

³Jiaozuo Coal Company, Henan Energy and Chemical Group Corporation, Jiaozuo 266590, China

⁴Tengdong Coal Company, Zaozhuang Mining Group Corporation, Zaozhuang 277519, China

Correspondence should be addressed to Lishuai Jiang; lsjiang@sdust.edu.cn and Xingyu Wu; WuXingyu1996@yeah.net

Received 24 February 2020; Revised 30 May 2020; Accepted 9 June 2020; Published 11 July 2020

Academic Editor: Filippo Ubertini

Copyright © 2020 Zequan Sun et al. This is an open access article distributed under the Creative Commons Attribution License, which permits unrestricted use, distribution, and reproduction in any medium, provided the original work is properly cited.

Dynamic and static coupling loads (DSLs) are one of the most common stress environments in underground engineering. As the depth of a roadway increases over the life of a mine, the static load of the ground stress field increase multiplies, and the cyclic operation at the working face releases a large amount of dynamic energy. Therefore, deep roadways easily induce dynamic disasters during production. In this paper, a deep roadway numerical model was built with FLAC^{3D} to test the deep roadway under DSLs and was simulated with 16 different support designs. The ground stability in each support condition was examined and compared in terms of the ground deformation and scope of failure. The underlying support mechanism was further analyzed with numerical modeling in view of the deformation in the surrounding rock mass induced by variations in the support parameters. The results show that shortening the bolt spacing is an effective measure to control the deformation of surrounding rock whatever DSLs or static load. Under static load, the larger the anchoring length is, the more stable the surrounding rock is. Under DSLs, end grouting length ($S = 600$ mm) and full grouting length ($S = 1800$ mm) can effectively control the deformation of surrounding rocks and enhance the stability of surrounding rocks. The results contribute to the design of supports in the field of underground coal mines and provide a basis for determining the reasonable support scheme for roadways.

1. Introduction

With the increase in energy demand and the increasing intensity of mining, shallow resources are decreasing, and the geological and geotechnical conditions of deep mining have become common in mines worldwide. Due to the high ground stress, high ground temperature, and high osmotic pressure, the geomechanical environment of the deep surrounding rock is significantly different from that in the shallow parts of the mine. As mining and underground constructions migrate to deeper levels, stress-induced rock fracturing and failure are inevitable. In some cases, rocks can fail, violently releasing a large amount of seismic energy and

causing damage in the form of dynamic disasters [1]. With the expansion of deep coal mining, dynamic disasters such as mine seismicity and rock bursts caused by mining are becoming increasingly prevalent. In deep underground excavations, high stress is the dominant feature for dynamic disaster conditions. However, geological factors can also be a significant contributor [2, 3]. Driad-Lebeau et al. [4, 5] analyzed the cause of a mine dynamic disaster in France. They found that the shock wave released the impact energy, indicating the correlation between the impact energy and the stress and elastic energy release rate. The research mentioned above has drawn a series of conclusions by analyzing the causes of dynamic disasters, the stress environment, and the

transformation of the mechanical properties of deep rock masses. In deep engineering, the excavation of roadways and working faces will damage the integrity of surrounding rock. The stress environment is changed, and the considerable mining space subjects deep roadways to high ground stress. The stress state and stability of roadways are significantly affected by the mining-induced stress distribution. The above factors have aggravated the occurrence of dynamic disasters in deep roadways.

In a deep roadway, under the joint action of the in situ stress and the mining-induced stress, the mining area and surrounding stress are in an extremely chaotic and unstable state [6–9]. When a certain amount of energy accumulates, a high-stress concentration zone will form. Cyclic operations at the working face, rock formation breakage, fault slip, and other dynamic events release shock waves that trigger the sudden release of elastic energy in the high-stress concentration zone, which induces large-area vibration of the rock formation and unstable failure. In the process of dynamic disasters, strong disturbance energy will be released, as well as complex original rock stress fields caused by deep mining. The abovementioned stresses jointly constitute the surrounding rock stress field of “high static load + strong disturbance” [10, 11]. Therefore, the energy type of most deep roadways is dynamic and static coupling loads. The dynamic load (D) comes from the strong disturbance energy released by the dynamic load. There are three main types of dynamic load in coal mines: (1) the energy generated by the propagation of shock waves in rock strata; (2) instantaneous load (passive dynamic load) generated by dynamic events such as rock formation breaking and fault slip; and (3) shock load generated by high-pressure gas in the center of explosive blasting. While the static load (S) comes from the stress field of the original rock caused by the strata overlying the deep roadway, the dynamic and static coupling loads are the most common stress environments in deep roadways. Therefore, the study of the mechanical response of surrounding rock in deep roadways under DSLs is of great significance for deep engineering. Some scholars have deeply divided the sources of deep dynamic loads in coal mines. Dou et al. proposed the principle and prevention of dynamic and static superimposed loads of coal mine [12]. He et al. conducted a numerical simulation study on rock burst induced by a hard roof [13, 14].

The main roadway serving the mining face is always located in the coal seam, which generally has relatively weak properties compared to those of the roof and floor rock strata. A database of coal mine rock mechanical properties, which consists of over 4,000 samples from fifty coal seams in ninety mines, was developed by Sun and Peng [15]. According to their work, most coal seams have a uniaxial compressive strength of less than 34 MPa and tensile strength of less than 2.7 MPa. Thus, it can be expected that the weak properties of coal contribute significantly to the stability of the surrounding rock (or it can be expected that the weak properties of coal are of great significance). The strata structure of the roadway in most coal mines is that the roof or floor is the weak strata, or the roadway is in the coal seam. Therefore, such a strata structure has far-reaching

significance for the study of the surrounding rock mechanical response of deep roadways under the loading of the DSLs.

With the further study of the bolting of deep roadways, new conclusions have been reached about the mechanical response of the deep roadway support under the DSL bolt. Mortazavi and Alavi [16] studied the response of the bolt with full grouting length under dynamic load. In this study, changes in bolt displacement acceleration and bolt pressure were recorded. Furthermore, the variation mechanism under the dynamic load was analyzed. Li et al. [17] proposed a dynamic simulation model for a cone bolt based on an experimental study; they performed drop weight tests on resin-based cone bolts. Their experiments revealed that the bolt has two energy absorption mechanisms: sliding in the resin and plastic deformation. These theories reveal the mechanical response of the bolt under the DSLs in detail and explain the mechanical method of the surrounding rock deformation controlled by the bolt in the dynamic load roadway. These theories reveal the mechanical response of one single bolt under the DSLs. For deep engineering scales, the response of the complete bolt support system can better reflect the mechanics of the surrounding rock in a deep roadway response.

To investigate the causes of the different ground control effects of the different support designs, a roadway-wide numerical model with a fine mesh was built, and the mechanism was analyzed from the perspective of support-induced tensile failure distributions and roof subsidence. In this study, the roadway stability with 16 different support designs under DSLs was investigated to determine the controlling effect of the four support parameters on ground deformation and failure. Further analysis of the simulation results has been conducted, which contributes to the stability analysis, support design, and optimization under DSL conditions.

2. Case Study

2.1. Geology and Geotechnical Overview of Zhaogu No. 2 Mine. Zhaogu No. 2 mine is located in Xinxiang City, Henan Province, China, was chosen as the study site because of the poor stability of its roadways. All panels in this mine are using retreating longwall method to extract coal seams. The coal seam is nearly horizontal with a mean thickness of 6.12 m.

The target gateroad for this case study is the roadway in 11050 panel at a depth of 800 m. The panel is approximately 180 m wide along the dip and 2000 m long along the strike as illustrated in Figure 1. A typical geological column based on core logging is shown in Figure 2. The roof strata of this panel are mainly composed of mudstone, sandy mudstone, and sandstone. The immediate roof is a layer of less than 2 m thick mudstone, which would cave and fall into the goaf, following the advance of coal extraction and shield support.

Bolt support simulates the method of prestressed bolts and strengthens the end support. The material of the bolt is high-strength steel bar, and the support scheme is shown in Figure 3. Density is 7500 kg/cm^3 , tensile strength is 225 kN,

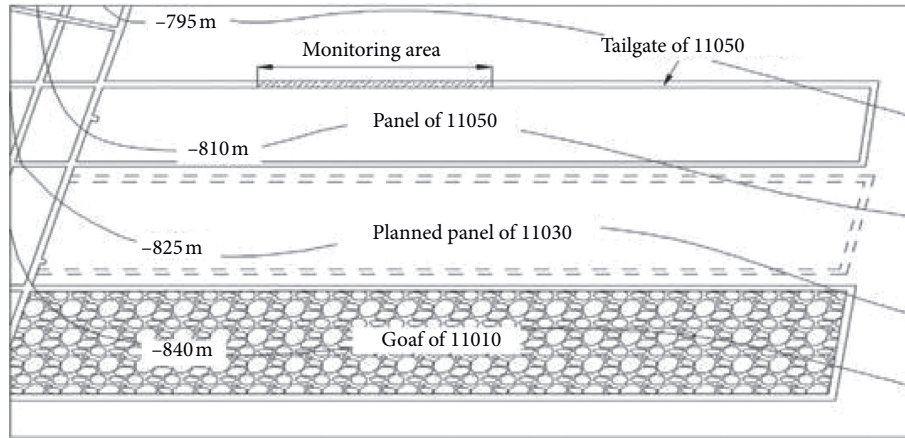


FIGURE 1: Plan view of local panel layout.

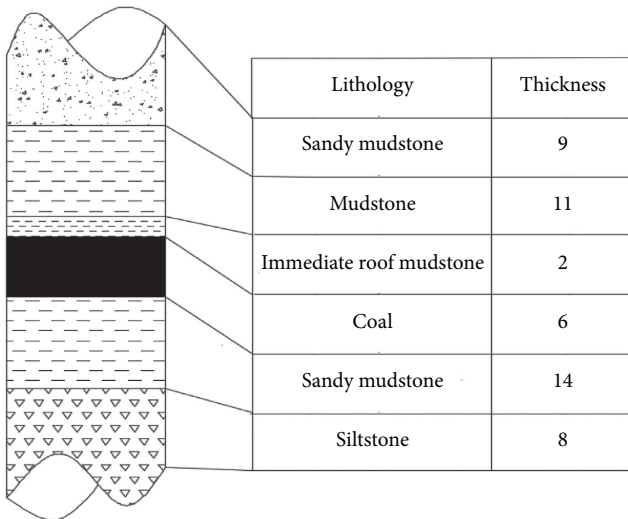


FIGURE 2: Typical geological column.

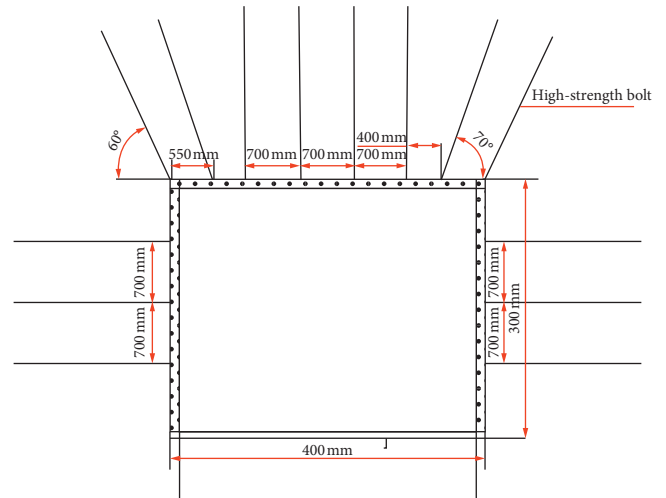


FIGURE 3: Roadway support schemes.

and Young’s modulus is 2.06 GPa. The bolt material elongation is 15%. The breaking load of the bolt material is 170 kN.

2.2. Establishment of a Numerical Model. In this study, the mining operations, including entry development, support installation, and coal-rock mass release energy, are simulated with FLAC^{3D}, a finite difference numerical simulation software suitable for rock support modeling with embedded structural elements. The numerical simulation model is shown in Figure 4. Currently, the nearly horizontal seam being mined is at a depth of approximately 800 m. As determined by model sensitivity analysis with regard to size and mesh density, the boundary conditions are set according to a previous numerical study of the same mine [18, 19]. The immediate roof and main roof of the target entry are composed of mudstone and sandy mudstone, respectively; two ribs and the floor are composed of coal because the entry was driven along the coal seam roofline. The roadway is 50 m long, 4 m wide, and 3 m high, as shown in Figure 1. The

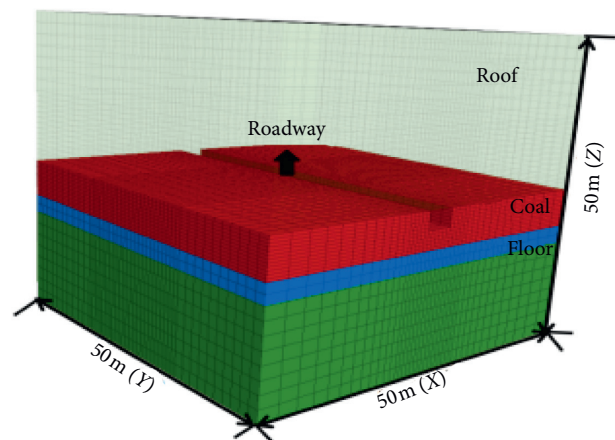


FIGURE 4: Numerical model.

model top boundary is loaded by a 20 MPa vertical stress to simulate the overburden pressure by assuming the overlying unit weight is 0.025 MN/m³, and no displacement is allowed

in the direction perpendicular to the side boundaries. The in situ stress is simulated by applying stresses of 22 and 16 MPa in the x - and y -directions, respectively. The model rock mass properties [20] are shown in Table 1.

After the completion of the support, the iterative calculation started again. After the simulation reaches the equilibrium, the dynamic analysis will proceed by applying dynamic load to the top of the model. According to previous scholars' modeling methods of dynamic load being only applied on the top surface of the model, the other surfaces of the model were set to static boundary conditions to absorb the stress waves of the dynamic load [21]. This process avoided the secondary dynamic destruction of the model by the internal refraction of the stress wave. Then, the dynamic calculation was used, and the model results were recorded when $T=0$ s, $T=0.02$ s, $T=0.04$ s, $T=0.06$ s, $T=0.08$ s, and $T=0.1$ s. The calculation was completed until the dynamic load was applied to 0.1 s. The numerical simulation process is shown in Figure 5.

The four factors of bolt length, bolt diameter, bolt spacing, and grouting length have a significant impact on the support effect. Four levels were set up under each factor, and 16 schemes were generated after optimizing the combination. The four factors were bolt length: 1800 mm, 2000 mm, 2200 mm, and 2400 mm; bolt diameter: 16 mm, 18 mm, 20 mm, and 22 mm; bolt spacing: 600 mm, 800 mm, 1000 mm, and 1200 mm; and grouting length: 600 mm, 1000 mm, 1400 mm, and 1800 mm (corresponding to grouting percentages of 30%, 50%, 70%, and 90%). In this study, the influence of a single bolt factor on the mechanical response of the surrounding rock was analyzed, thus providing a data analysis basis for the optimization of the DSL soft rock roadway support. The support schemes are shown in Table 2.

2.3. Determination of the Dynamic Load. In underground mining activities, the determination of the location of the dynamic load source has specific technical difficulties. The location selection of the source has a significant influence on the surrounding rock of the roadway [20, 21]. It is better to choose the simulated dynamic vibration wave to transmit energy in the surrounding rock. Most deep engineering dynamic disasters are mainly caused by the transmission of shock waves in the rock formation. Therefore, the model selects the dynamic load application method as a surface application instead of the point-source application. The dynamic load damping is mainly caused by the internal friction of the material and the possible sliding of the contact surface. To reproduce the damping of the natural system under the dynamic load in the numerical simulation, the model adopts the Rayleigh damping setting method. According to previous scholars' calculation methods of *QUAD4 Rayleigh* damping, we can know that when the damping ratio is 5%, the damping ratio at this time is a damping ratio independent of the dynamic frequency of the dynamic load. The damping ratio of 5% was chosen to offset the uncontrollable energy transfer caused by the different depths of the model rock layer and the frequency of the

dynamic load [22–24]. The effect of the dynamic load has periodicity, and the dynamic energy of the simulated dynamic load derives from the periodic disturbance of mining at the working face. Thus, the other parameters of the experimental dynamic load are determined by taking the working face mining disturbance as an example to determine the relevant parameters of the dynamic load. First, the dynamic load of the mining activity is regarded as a shock wave, which is added to the internal nodes of the model in a speed-time course. It can be seen from the theory of an elastic wave that any shock wave can be synthesized by Fourier transformation using several sine waves. Hence, the sine wave is the basic form of the shock wave.

For the sinusoidal shock wave transmitted in the z direction, the particle velocity $v(z, t)$ is from the following equation:

$$v(z, t) = v_0 \sin\left[2\pi f\left(\frac{t-z}{c}\right)\right], \quad (1)$$

where v_0 is the maximum vibration velocity of the particle (maximum amplitude of peak velocity), f is the shock wave frequency, and C is the shock wave velocity. t is the time it takes for the shock wave to cycle once, and z is the propagation speed of the shock wave in the z -axis direction.

Some research has calculated and analyzed the micro-seism events of coal mines with different energy levels [25] and found a larger maximum peak velocity but a lower vibration frequency. When the vibration energy is $1e^4-1e^5$, the vibration frequency is 2–15; when the vibration energy is $1e^5-1e^6$, the vibration frequency is 0.5–12; and when the vibration energy is greater than $1e^6$, the vibration frequency is 0.4–5. The action time of the shock wave takes one cycle of the simple harmonic, which is $T=1/f$. Because $f=10$ Hz in the simulation, the corresponding energy level is $1e^4-1e^5$, which meets the range of the dynamic load energy level in the literature [25]. The magnitude of T is 0.1 s in one cycle. The action time is 0.1 s for one cycle.

From [25], we can determine the strain rate of coal mine dynamic disasters, as shown in Table 3. Because the corresponding energy level of the shock wave is $1e^4-1e^5$ and 3, 4, and 5 in Table 3 are all within this energy level range, the middle value of the wave speed range of the three experimental groups is selected to determine the wave speed to 2.5 m/s.

3. Parametric Study of Support Parameters on Roadway Ground Behavior

3.1. Influence of Bolt Length on the Response of Roadway Rock. The plastic zone distribution scope of the roadway and subsidence of the roof are the most common and direct indicators for the evaluation of roof stability and roof support design. The parameters of the support bolt are L (bolt length), φ (bolt diameter), L_g (bolt spacing), and S (grouting length). In this simulation, four levels were selected for the support parameters and the impact of variation in the parameters on the surrounding rock of the roadway under dynamic and static loading was studied. The simulated parameters are shown in Table 4.

TABLE 1: Rock mass properties.

Stratum	Lithology	σ_t (MPa)	Φ (deg)	E_i (GPa)	V	γ (kg·m ⁻³)	K (GPa)
Roof	Sandy mudstone	2.10	35	1.40	0.25	2770	5.3
	Mudstone	1.97	34	3.10	0.29	2552	2.9
	Immediate roof mudstone	1.40	28	1.40	0.24	2552	2.9
Coal seam	Coal	1.30	31	0.60	0.30	1450	0.67
Floor	Sandy mudstone	3.43	36	5.13	0.27	2852	7.4
	Siltstone	4.13	47	7.13	0.22	2961	9.6

σ_t is the tensile strength, Φ is the friction angle, E_i is the elastic modulus, V is Poisson's ratio, γ is the density of rock, and K is the bulk modulus.

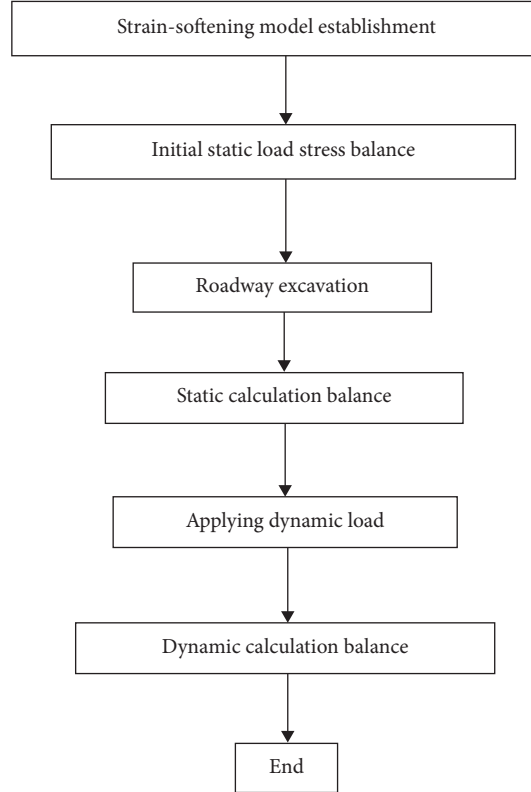


FIGURE 5: Flow chart of the numerical simulation.

TABLE 2: Simulation support design schemes.

Design mark	Variable	Constants	Number of design
Design L	Rock bolt length (L)	Rock bolt diameter Rock bolt spacing Grouting length	4
Design φ	Rock bolt diameter (φ)	Rock bolt length Rock bolt spacing Grouting length	4
Design Lg	Rock bolt spacing (Lg)	Rock bolt length Rock bolt diameter Grouting length	4
Design S	Grouting length (S)	Rock bolt length Rock bolt diameter Rock bolt spacing	4

Figure 6 and Table 5 show that Design L_1 and Design L_2 ($L=1800$ mm and $L=2000$ mm, respectively) have the widest distribution of tensile failure zones. By applying an

increase in L , the number of tensile failure zones in the roadway decreases dramatically: 13.1% failure reduction for Design L_3 and 13.8% reduction for Design L_4 under the static

TABLE 3: Range of the dynamic load strain rate of coal mine dynamic disasters.

Number	E (J)	F (Hz)	Pv (m/s)	SR (s^{-1})
1	1240	3~25	0.20~0.84	$1.5 \times 10^{-3} \sim 5.3 \times 10^{-2}$
2	8270	2~18	0.34~1.00	$1.7 \times 10^{-3} \sim 4.6 \times 10^{-2}$
3	22600	2~18	0.79~3.44	$4.0 \times 10^{-3} \sim 1.6 \times 10^{-1}$
4	27100	1~15	0.44~3.50	$1.1 \times 10^{-3} \sim 1.3 \times 10^{-1}$
5	50400	2.5~15	0.50~3.27	$3.2 \times 10^{-3} \sim 1.2 \times 10^{-1}$
6	103000	0.5~12	1.23~3.65	$1.6 \times 10^{-3} \sim 1.1 \times 10^{-1}$
7	3970000	0.4~5	8.45~12.27	$8.6 \times 10^{-3} \sim 1.6 \times 10^{-1}$

E is the energy, F is the frequency, Pv is the peak velocity, and SR is the strain rate.

TABLE 4: Model design with different bolt lengths.

Model	L (mm)	φ (mm)	Lg (mm)	S (mm)
L_1	1800	20	1000	900
L_2	2000	20	1000	1000
L_3	2200	20	1000	1100
L_4	2400	20	1000	1200

L is the bolt length, φ is the bolt diameter, Lg is the bolt spacing, and S is the grouting length.

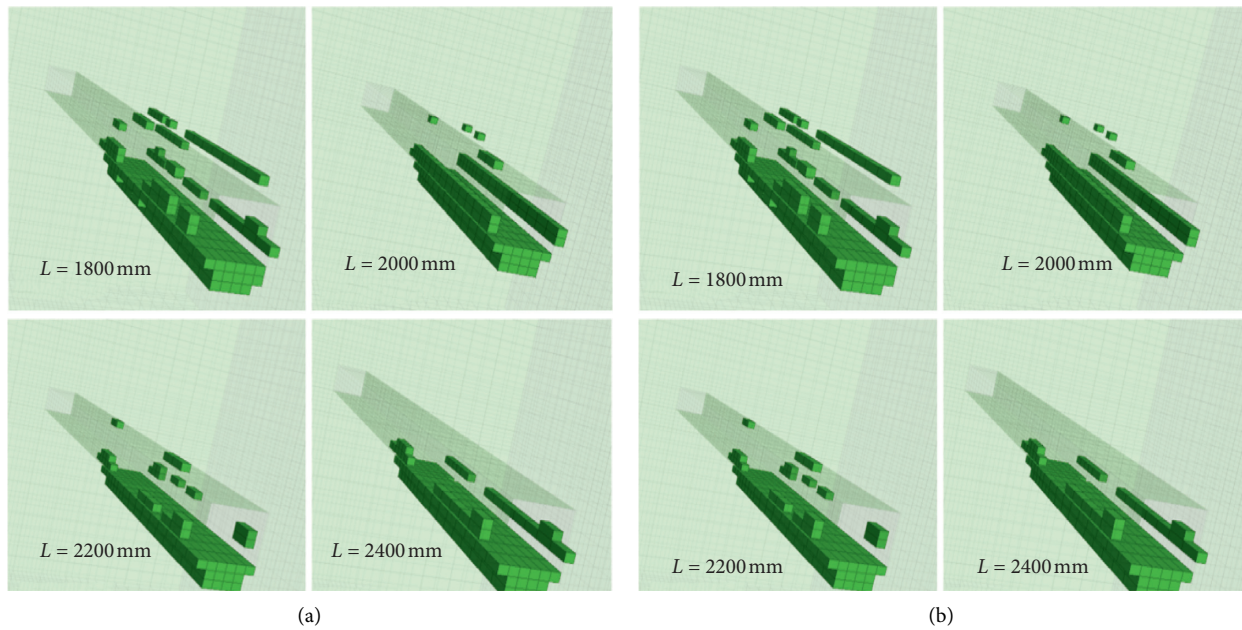
FIGURE 6: Roadway tensile failure distribution with different bolt lengths: (a) $T=0$ s; (b) $T=0.1$ s.

TABLE 5: Number of tensile failures with different bolt lengths.

Dynamic time (s)	Number of tensile failures			
	$L=1800$ mm	$L=2000$ mm	$L=2200$ mm	$L=2400$ mm
$T=0.00$ s	800	792	695	680
$T=0.02$ s	800	792	695	680
$T=0.04$ s	2067	1848	1856	1940
$T=0.06$ s	2252	2040	2045	2103
$T=0.08$ s	2507	2431	2255	2248
$T=0.10$ s	2517	2448	2277	2260

load. Under the DSLs, the number of tensile failure zones in the roadway has been decreased by 257. In addition to the control effect in the number of tensile failures, as shown in Figure 6, the scope of the tensile failure between the roof and two ribs is controlled by enhancing L . Similar to the subsidence results, Design L_3 and Design L_4 show certain control of the tensile failure scope in the roof and two ribs.

In addition to the control of the tensile failure scope, as shown in Table 6, the roof subsidence was also reduced by enhancing L . In comparison to the results of Design L_1 , the roof subsidence of Design L_3 and Design L_4 is reduced by 5.18 mm and 9.02 mm, respectively, under the DSLs, and roof subsidence exhibits no significant effect under the static load.

3.2. Influence of Bolt Diameter on the Response of the Rock Surrounding the Roadway. By using the diameter of the bolt as the simulated variable, the bolt diameter simulation was established for four sets. The bolt diameters of the four sets were 16 mm, 18 mm, 20 mm, and 22 mm. The support parameters are shown in Table 7.

Figure 7 and Table 8 show all the simulated results of Design φ . By increasing φ , the number of tensile failure zones in the roadway did not decrease dramatically. The results of the four sets of simulations are highly similar. As shown in Figure 7, the roadway tensile failure distribution is highly consistent under the static load or DSLs. Table 8 shows that the differences in the support effects of the four sets of simulations under the DSLs or static load were all within 100.

Table 9 shows that the differences in the four sets of roof subsidence simulations under the DSLs or static load were all within 1 mm. Changing the diameter of the bolt has less impact on the roof subsidence.

3.3. Influence of the Bolt Spacing on the Response of the Rock Surrounding the Roadway. By using the spacing of the bolt as the simulated variable, the bolt spacing simulation was established for four sets. The bolt spacings of the four sets were 600 mm, 800 mm, 1000 mm, and 1200 mm. The support parameters are shown in Table 10.

Figure 8 and Table 11 show that Design Lg_3 and Design Lg_4 ($Lg=1000$ mm and $Lg=12000$ mm) have the widest distribution of tensile failure zones. By shortening Lg , the number of tensile failure zones in the roadway decreases dramatically: 31.9% reduction in failures for Design Lg_1 and 29.3% reduction for Design Lg_2 under the static load. Under the DSLs, the number of tensile failure zones in the roadway similarly decreases with a 41.1% failure reduction for Design Lg_1 and 39.9% reduction for Design Lg_2 . In addition to the control effects in the number of tensile failures, as shown in Figure 8, the scope of the tensile failure between the roof and two ribs is controlled by shortening Lg . Similar to the subsidence results, Design Lg_1 and Design Lg_2 show certain control of the extent of tensile failure in the roof and two ribs.

In addition to the control of the scope of tensile failure, as shown in Table 12, the roof subsidence was also reduced by shortening Lg . In comparison to the results of Design Lg_4 ,

the roof subsidence values of Design Lg_1 and Design Lg_2 are reduced by 35.59 mm (20.5%) and 18.53 mm (10.7%) under the DSLs, respectively, and by 29.56 mm (38.0%) and 24.18 mm (31.1%) under the static load, respectively. Regardless of the type of load, the Lg has a significant effect on roof subsidence.

3.4. Influence of the Grouting Length on the Response of the Rock Surrounding the Roadway. By using the grouting length as the simulated variable, the grouting length simulation was established for four sets. The bolt grouting lengths of the four sets were 600 mm, 1000 mm, 1400 mm, and 1800 mm. The support parameters are shown in Table 13.

Figure 9 and Table 14 show that Design S_1 ($S=600$ mm) has the widest distribution of tensile failure zones under the static load. By increasing S , the number of the tensile failure zones in the roadway decreases dramatically: a 20.3% reduction in failures unit obtained for Design S_4 under the static load. In addition, new simulation results indicate that Design S_2 and Design S_3 ($S=1000$ mm and $S=1400$ mm) have the widest distribution of tensile failure zones under the DSLs. In comparison to the results of Design S_2 , the number of tensile failure zones in the roadway of Design S_1 and Design S_4 is reduced by 319 (14.2%) and 203 (9.0%), respectively, under the DSLs.

The roof subsidence was also reduced by enhancing S . In comparison to the results of Design S_1 , the roof subsidence of Design S_4 was reduced by 25.84 mm (31.59%) under the static load. Table 15 shows that the roof subsidence decreases with increasing grouting length under static load. However, when the stress condition becomes DSLs, the variation in roof deformation is the same as that of the tensile failure zone. Design S_2 ($S=1000$ mm) has the largest roof subsidence under the DSLs. In comparison to the results of Design S_2 , the roof subsidence values of Design S_1 and Design S_4 are reduced by 7.04 mm (4.1%) and 11.61 mm (6.8%), respectively, under the DSLs.

4. Analysis of the Support Designs

It can be concluded from the simulation results in Section 3 that the difference between Design L and Design φ is not significant in terms of the control effects on the roof subsidence and the tensile failure distribution and quantities. However, one interesting point worth noting is that although L and φ do not have significant control effects on the roof subsidence and the tensile failure distribution and quantities, in this simulation of four factors, the tensile failure is closely associated with roof subsidence. Roadways with small amounts of roof subsidence usually have small numbers of tensile failures and small distribution scopes.

Design Lg has a significant effect on the roof subsidence and the tensile failure quantities and distribution under the static load or DSLs. Shortening Lg is an effective way to increase the stability of the roadway under both static and DSL conditions. According to the suspension theory [26], the purpose of the bolt is to suspend the weak or severely

TABLE 6: Roof subsidence with different bolt lengths.

Dynamic time (s)	Roof subsidence (mm)			
	$L = 1800$ mm	$L = 2000$ mm	$L = 2200$ mm	$L = 2400$ mm
$T = 0.00$ s	56.73	56.27	57.83	57.65
$T = 0.02$ s	56.68	56.34	57.87	57.65
$T = 0.04$ s	65.42	67.81	67.09	66.34
$T = 0.06$ s	77.82	77.22	75.64	74.06
$T = 0.08$ s	111.53	110.70	108.72	106.30
$T = 0.10$ s	174.89	171.14	169.71	165.87

TABLE 7: Model design with different bolt diameters.

Model	L (mm)	φ (mm)	L_g (mm)	S (mm)
φ_1	2000	16	1000	1000
φ_2	2000	18	1000	1000
φ_3	2000	20	1000	1000
φ_4	2000	22	1000	1000

φ is the bolt diameter, L is the bolt length, L_g is the bolt spacing, and S is the grouting length.

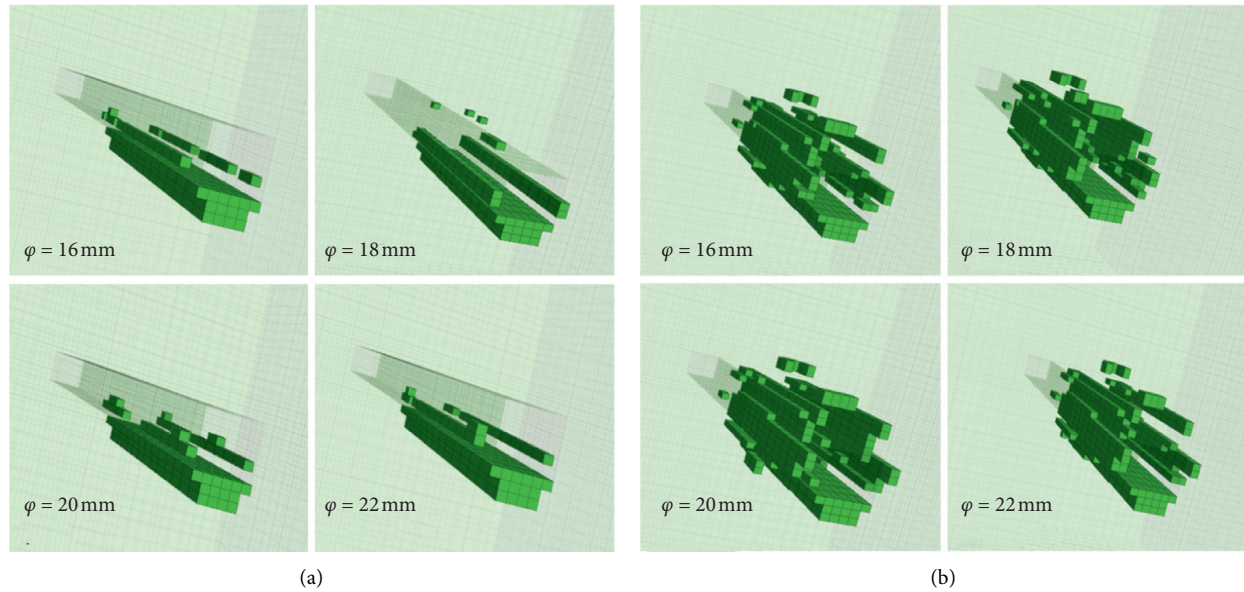


FIGURE 7: Roadway tensile failure distribution with different rock bolt diameters: (a) $T = 0$ s; (b) $T = 0.1$ s.

TABLE 8: Number of tensile failures with different bolt diameters.

Dynamic time (s)	Number of tensile failures			
	$\varphi = 16$ mm	$\varphi = 18$ mm	$\varphi = 20$ mm	$\varphi = 22$ mm
$T = 0.00$ s	680	679	692	741
$T = 0.02$ s	680	679	692	741
$T = 0.04$ s	1791	1802	1848	1870
$T = 0.06$ s	1972	1989	2040	2028
$T = 0.08$ s	2149	2145	2231	2235
$T = 0.10$ s	2169	2177	2248	2261

TABLE 9: Roof subsidence with different bolt diameters.

Dynamic time (s)	Roof subsidence (mm)			
	$\varphi = 16$ mm	$\varphi = 18$ mm	$\varphi = 20$ mm	$\varphi = 22$ mm
$T = 0.00$ s	56.10	56.90	56.34	55.87
$T = 0.02$ s	56.10	56.99	56.34	55.89
$T = 0.04$ s	69.66	68.87	67.81	67.32
$T = 0.06$ s	78.08	77.88	77.22	77.00
$T = 0.08$ s	111.80	110.05	110.70	110.44
$T = 0.10$ s	171.55	171.40	171.14	170.40

broken rock on the overlying hard rock to maintain the integrity of the surrounding rock. After shortening L_g , the number of bolts suspended in the hard rock strata increases, which dramatically increases the strength of the surrounding

rock grouting area, and the maximum load limit of the supporting system is significantly increased, thereby controlling the surrounding rock deformation and increasing the stability of the roadway.

TABLE 10: Model design with different bolt spacings.

Model	L (mm)	φ (mm)	L_g (mm)	S (mm)
Lg_1	2000	20	600	1000
Lg_2	2000	20	800	1000
Lg_3	2000	20	1000	1000
Lg_4	2000	20	1200	1000

L_g is the bolt spacing, L is the bolt length, φ is the bolt diameter, and S is the grouting length.

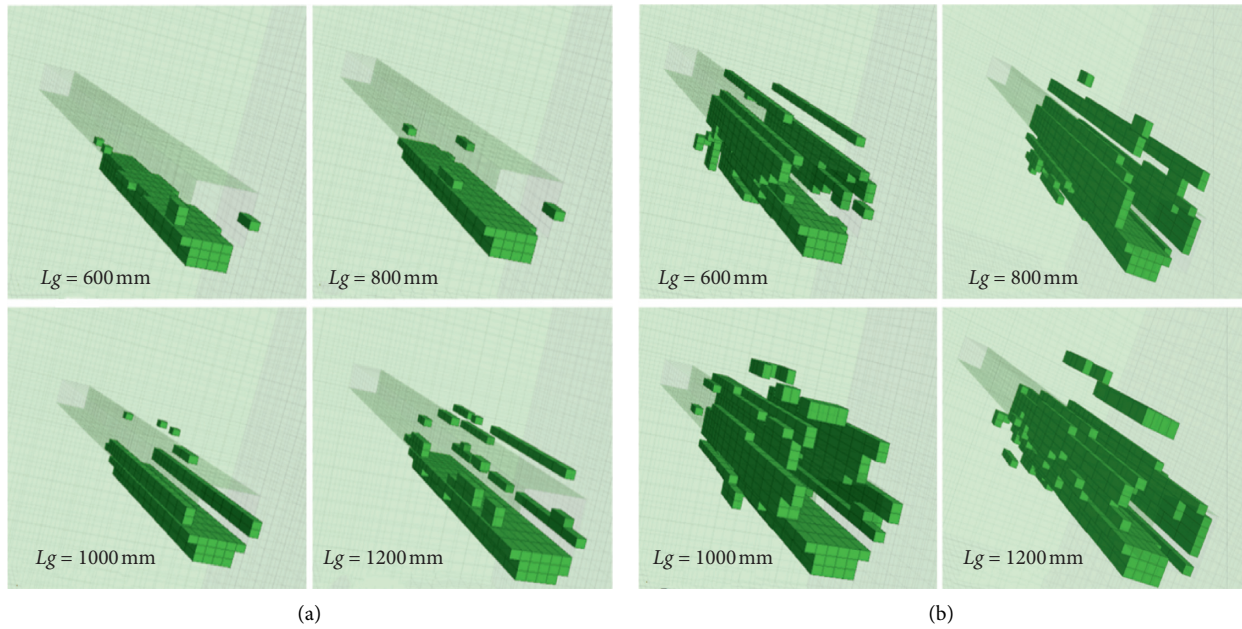


FIGURE 8: Roadway tensile failure distribution with different rock bolt spacings: (a) $T = 0$ s; (b) $T = 0.1$ s.

TABLE 11: Number of tensile failures with different bolt spacings.

Dynamic time (s)	Number of tensile failures			
	$L_g = 600$ mm	$L_g = 800$ mm	$L_g = 1000$ mm	$L_g = 1200$ mm
$T = 0.00$ s	599	617	692	873
$T = 0.02$ s	599	617	692	873
$T = 0.04$ s	1278	1509	1848	1918
$T = 0.06$ s	1433	1594	2040	2095
$T = 0.08$ s	1702	1725	2231	2733
$T = 0.10$ s	1710	1741	2248	2897

TABLE 12: Roof subsidence with different bolt spacings.

Dynamic time (s)	Roof subsidence (mm)			
	$L_g = 600$ mm	$L_g = 800$ mm	$L_g = 1000$ mm	$L_g = 1200$ mm
$T = 0.00$ s	48.26	53.64	56.27	77.82
$T = 0.02$ s	48.30	53.68	56.34	77.92
$T = 0.04$ s	50.87	62.32	67.81	76.65
$T = 0.06$ s	55.68	70.35	77.22	79.81
$T = 0.08$ s	81.07	101.44	110.70	101.81
$T = 0.10$ s	138.28	155.34	171.14	173.87

TABLE 13: Model design with different grouting lengths.

Model	L (mm)	φ (mm)	L_g (mm)	S (mm)
S_1	2000	20	1000	600
S_2	2000	20	1000	1000
S_3	2000	20	1000	1400
S_4	2000	20	1000	1800

S is the grouting length, L is the bolt length, φ is the bolt diameter, and L_g is the bolt spacing.

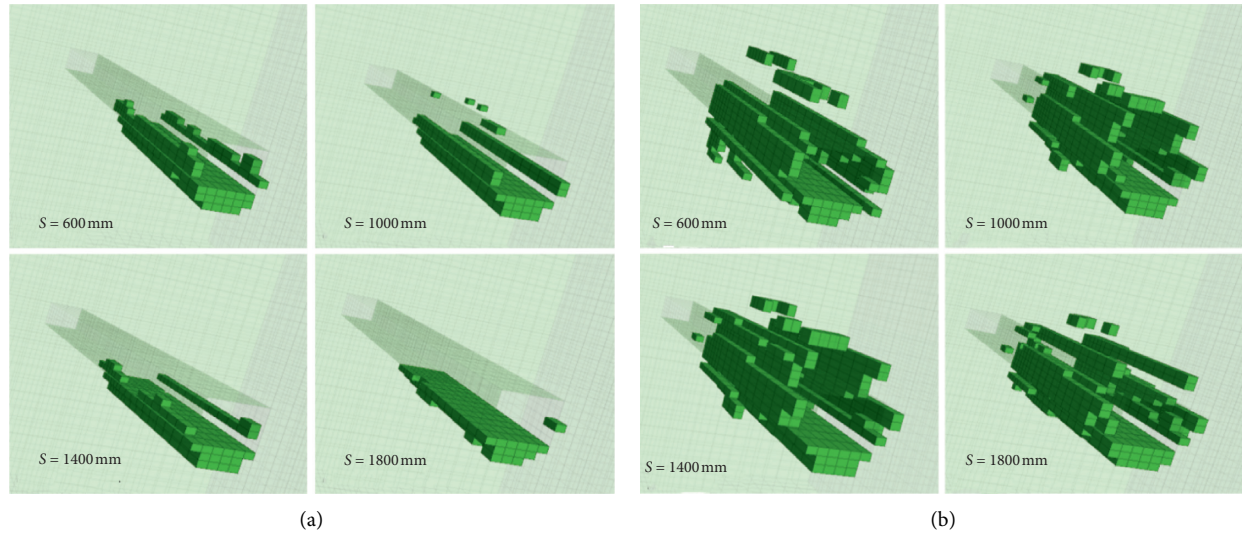
FIGURE 9: Roadway tensile failure distribution at different grouting lengths: (a) $T = 0$ s; (b) $T = 0.1$ s.

TABLE 14: Number of tensile failures with different grouting lengths.

Dynamic time (s)	Number of tensile failures			
	$S = 600$ mm	$S = 1000$ mm	$S = 1400$ mm	$S = 1800$ mm
$T = 0.00$ s	871	692	690	694
$T = 0.02$ s	871	692	690	694
$T = 0.04$ s	1596	1848	1840	1747
$T = 0.06$ s	1797	2040	1996	1831
$T = 0.08$ s	1849	2231	2176	1917
$T = 0.10$ s	1929	2248	2192	2045

Design S provides an interesting simulation result on the DSLs. The roof subsidence values of Design S_1 is 32 mm more than that of Design S_2 under static load, but the roof subsidence value of Design S_1 under DSLs has decreased by nearly 10 mm compared to the Design S_2 . And, under the DSLs, Design S_2 has the most tensile failure zones and largest roof subsidence. In comparison to the results of Design S_2 , the roof subsidence values of Design S_1 and Design S_4 are reduced by 7.04 mm (4.1%) and 11.61 mm (6.8%) under DSLs. In this simulation, Design S_1 has the worst stability under the static load. In contrast, when the dynamic load acts on the roadway, Design S_1 has the minimum amount of roof subsidence, number of tensile failures, and smallest distribution. When $S = 600$ mm, the roof has massive settlement subsidence under the static load. In addition, the roof cannot bear a high-stress concentration, and a mass of

TABLE 15: Roof subsidence with different grouting lengths.

Dynamic time (s)	Roof subsidence (mm)			
	$S = 600$ mm	$S = 1000$ mm	$S = 1400$ mm	$S = 1800$ mm
$T = 0.00$ s	81.79	56.27	55.86	55.95
$T = 0.02$ s	81.79	56.34	55.96	56.03
$T = 0.04$ s	80.72	67.81	66.05	67.47
$T = 0.06$ s	84.18	77.22	75.95	76.83
$T = 0.08$ s	99.51	110.70	109.87	110.23
$T = 0.10$ s	164.10	171.14	170.12	159.53

the stress shifts to the deep part of the surrounding rock to achieve a specific effect of surrounding rock pressure relief [26]. Moreover, when subjected to dynamic load, the lengthening of the steel bar leads to a decrease in diameter whereby the outer end of the bolt is free to yield. The rock bolt has a weak plastic deformation capacity when fully grouted in cement. Therefore, the low grouting design creates plastic deformation in the bolt. In a laboratory, rock bolts in concrete cylinders were subjected to free tests to achieve a loading velocity of 10 m/s. The tests demonstrated that the distribution of plastic strain along the length of a grouted rock bolt is not constant when dynamically loaded. The section where plastic yielding was allowed was not fully utilized in any of the cases, opposite to the results in previous static tests that show almost constant elongation of the bolts. The tests also verified that the load-carrying components of the bolt, the nut, and the grouting are reliable when

dynamically loaded [27]. Thus, Design S_1 achieves flexible support, reduces the damage to the surrounding rock from shock waves, and has a good simulation result in the DSLs [28–30]. However, Design S_1 has no obvious improvement effect under static and static superimposed load. However, the above results show that the support Design S_1 is suitable for surrounding rock deformation control under DSLs. Flexible support and timely pressure relief can be used as effective control measures for surrounding rock deformation of DSL roadway [31–34]. When large area of surrounding rock deformation occurs in DSLs roadway, these two measures can be used reasonably to enhance the stability of DSLs surrounding rock. This simulation provides reasonable simulation data for roadway support design under DSLs.

5. Conclusions

In this study, the roadway stability with 16 different support designs under DSLs was investigated with a roadway-wide numerical model. A parametric study was conducted to investigate the controlling effects of the four support parameters on ground deformation and failure. Further analysis of the simulation results has been conducted, which contributes to the stability analysis, support design, and optimization under DSL conditions.

According to the simulation results, both Design S and L_g can reduce the extent of the failure of the surrounding rock mass. After shortening L_g , the number of bolts suspended in the hard rock strata increases, which dramatically increases the strength of the surrounding rock grouting area, and the maximum load limit of the supporting system is significantly increased, thereby controlling the surrounding rock deformation and increasing the stability of the roadway. In Design S , under static load, Design S_1 has the most tensile failure zones and largest roof subsidence. Design S_4 is to increase the upper limit of the load of the surrounding rock support system by increasing the anchor length. Design S_1 is to enhance the stability of surrounding rocks through flexible support and timely pressure relief. All two support designs have obtained good simulation results under DSLs. Simulation results of Design S_1 show that flexible support and timely pressure relief can be used as effective control measures for surrounding rock deformation of DSL roadway.

To investigate the causes of the different ground control effects of the different support designs, a roadway-wide numerical model with a fine mesh was built, and the mechanism was analyzed from the perspective of support-induced tensile failure distributions and roof subsidence. First, all simulation results indicate that tensile failure and roof subsidence have a consanguineous correlation. Roadways with small amounts of roof subsidence usually have small numbers of tensile failures and small distribution scopes. These two indicators reflect the stability of the rock surrounding the roadway. In addition, L_g (bolt spacing) and S (grouting length) have significant control effects on the roadway rock mass. L_g has significant control effects under both stress conditions. Shortening L_g is an effective way to increase the stability of the roadway and control rock

deformation. All the Design S simulation results under the DSLs indicate that the rock pressure relief and the bolt plastic deformation capacity are important factors that affect the stability of roadway under DSL conditions. In the process of support design optimization under the DSLs, the rock pressure relief and the bolt plastic deformation capacity should be considered. These four factors (shortening bolt spacing, high grouting length, rock pressure relief, and bolt plastic deformation capacity) significantly influence the DSL roadway. These factors can provide a basis for determining a reasonable support scheme for the DSL roadway.

Data Availability

The processed data required to reproduce these findings cannot be shared at this time as the data also form part of an ongoing study.

Conflicts of Interest

The authors declare that there are no conflicts of interest regarding the publication of this paper.

Acknowledgments

This study was sponsored by the National Natural Science Foundation of China (51704185 and 51774195), the Natural Science Foundation of Shandong Province (ZR2017BEE045 and ZR2017BEE050), and the Shandong Key Laboratory of Civil Engineering Disaster Prevention and Mitigation (CDPM2019KF08).

References

- [1] P. K. Kaiser, D. D. Tannant, and D. R. McCreath, *Canadian Rockburst Support Handbook*, p. 314, Geomechanics Research Centre, Laurentian University, Sudbury, Ontario, Canada, 1996.
- [2] W. Gong, Y. Peng, H. Wang, M. He, L. Ribeiro e Sousa, and J. Wang, "Fracture angle Analysis of rock burst faulting planes based on true-triaxial experiment," *Rock Mechanics and Rock Engineering*, vol. 48, no. 3, pp. 1017–1039, 2015.
- [3] M. He, L. R. Sousa, T. Miranda, and G. Zhu, "Rockburst laboratory tests database—application of data mining techniques," *Engineering Geology*, vol. 185, pp. 116–130, 2015.
- [4] L. Driad-Lebeau, F. Lahaie, M. Al Heib, J. P. Josien, P. Bigarré, and J. F. Noirel, "Seismic and geotechnical investigations following a rockburst in a complex French mining district," *International Journal of Coal Geology*, vol. 64, no. 1-2, pp. 66–78, 2005.
- [5] L. Jiang, P. Kong, P. Zhang et al., "Dynamic analysis of the rock burst potential of a longwall panel intersecting with a fault," *Rock Mechanics and Rock Engineering*, vol. 53, no. 4, pp. 1737–1754, 2020.
- [6] A. Sainoki and H. S. Mitri, "Dynamic modelling of fault-slip with Barton's shear strength model," *International Journal of Rock Mechanics and Mining Sciences*, vol. 67, pp. 155–163, 2014.
- [7] P. Kong, L. Jiang, J. Jiang, Y. Wu, L. Chen, and J. Ning, "Numerical analysis of roadway rock-burst hazard under superposed dynamic and static loads," *Energies*, vol. 12, no. 19, p. 3761, 2019.

- [8] L. Dou and L. Lu, "The strength weakening and subtraction theory of impact rock pressure and its application," *Journal of China Coal Society*, vol. 6, pp. 690–694, 2005.
- [9] W. Cai, "The principle of dynamic and static load superposition induction and monitoring and early warning research of fault-type rock burst," Doctoral dissertation, 2015.
- [10] X. B. Li, Y. J. Zuo, and C. Ma, "Strain energy density criterion and catastrophe theory analysis of rock failure under dynamic and static loading," *Journal of Rock Mechanics and Engineering*, vol. 24, no. 16, pp. 2814–2824, 2005.
- [11] P. Kong, L. Jiang, J. Shu, A. Sainoki, and Q. Wang, "Effect of fracture heterogeneity on rock mass stability in a highly heterogeneous underground roadway," *Rock Mechanics and Rock Engineering*, vol. 52, no. 11, pp. 4547–4564, 2019.
- [12] L. M. Dou, J. He, A. Cao, S. Gong, and W. Cai, "The principle of dynamic and static load superposition and its prevention in coal mine impacting mines," *Journal of China Coal Society*, vol. 7, pp. 5–12, 2015.
- [13] J. He, L.-m. Dou, Z.-l. Mu, A.-y. Cao, and S.-y. Gong, "Numerical simulation study on hard-thick roof inducing rock burst in coal mine," *Journal of Central South University*, vol. 23, no. 9, pp. 2314–2320, 2016.
- [14] J. He and L. Dou, "Mechanism of induced rock pressure induced by a dynamic and static combination of the thin coal seam," *Journal of China Coal Society*, vol. 39, no. 11, pp. 2177–2182, 2014.
- [15] C. Sun and S. Peng, "Rock mechanics property data bank for coal measure strata," in *Proceedings of 12th International Conference On Ground Control in Mining: Department of Mining Engineering, College of Mineral and Energy Resources, West Virginia University*, pp. 330–341, Morgantown, WV, USA, August 1993.
- [16] A. Mortazavi and F. T. Alavi, "A numerical study of the behavior of fully grouted rockbolts under dynamic loading," *Soil Dynamics and Earthquake Engineering*, vol. 54, pp. 66–72, 2013.
- [17] Z.-l. Li, X.-q. He, L.-m. Dou, D.-z. Song, G.-f. Wang, and X.-l. Xu, "Investigating the mechanism and prevention of coal mine dynamic disasters by using dynamic cyclic loading tests," *Safety Science*, vol. 115, pp. 215–228, 2019.
- [18] L. Jiang, A. Sainoki, H. S. Mitri, N. Ma, H. Liu, and Z. Hao, "Influence of fracture-induced weakening on coal mine gateroad stability," *International Journal of Rock Mechanics and Mining Sciences*, vol. 88, pp. 307–317, 2016.
- [19] L. Jiang, H. S. Mitri, N. Ma, and X. Zhao, "Effect of foundation rigidity on stratified roadway roof stability in underground coal mines," *Arabian Journal of Geosciences*, vol. 9, no. 1, p. 32, 2016.
- [20] L. Jiang, P. Zhang, L. Chen et al., "Numerical approach for goaf-side entry layout and yield pillar design in fractured ground conditions," *Rock Mechanics and Rock Engineering*, vol. 50, no. 11, pp. 3049–3071, 2017.
- [21] J. He, L.-M. Dou, W. Cai, Z.-L. Li, and Y.-L. Ding, "In situ test study of characteristics of coal mining dynamic load," *Shock and Vibration*, vol. 2015, Article ID 121053, 8 pages, 2015.
- [22] S. J. Chen, D. W. Yin, N. Jiang, F. Wang, and W. J. Guo, "Simulation study on effects of loading rate on uniaxial compression failure of composite rock-coal layer," *Geomechanics and Engineering*, vol. 17, no. 4, pp. 333–342, 2019.
- [23] I. M. Idriss, J. Lysmer, R. Hwang et al., "QUAD4: a computer program for evaluating the seismic response of soil structures by variable damping finite element procedures," University of California, Berkeley, CA, USA, EERC 73-16, 1973.
- [24] D. G. Zou, B. Xu, and X. J. Kong, "Study of influence of determining Rayleigh damping coefficient on seismic response of high earth-rock dams," *Rock and Soil Mechanics*, vol. 32, no. 3, pp. 797–803, 2011.
- [25] J. He, "Research of mining dynamic loading effect and its induced rock burst in coal mine," Doctoral dissertation, China University of Mining and Technology, Xuzhou, China, 2013.
- [26] B. H. G. Brady and E. T. Brown, *Rock Mechanics for Underground Mining*, Springer, Dordrecht, Netherlands, 1985.
- [27] A. Ansell, "Laboratory testing of a new type of energy absorbing rock bolt," *Tunnelling and Underground Space Technology*, vol. 20, no. 4, pp. 291–300, 2005.
- [28] P. K. Kaiser and M. Cai, "Design of rock support system under rockburst condition," *Journal of Rock Mechanics and Geotechnical Engineering*, vol. 4, no. 3, pp. 215–227, 2012.
- [29] L. Jiang, Q. Wu, Q. Wu et al., "Fracture failure analysis of hard and thick key layer and its dynamic response characteristics," *Engineering Failure Analysis*, vol. 98, pp. 118–130, 2019.
- [30] Y. Li, C. Tang, D. Li, and C. Wu, "A new shear strength criterion of three-dimensional rock joints," *Rock Mechanics and Rock Engineering*, vol. 53, no. 3, p. 1477, 2020.
- [31] Q. Liu, J. Chai, S. Chen, D. Zhang, Q. Yuan, and S. Wang, "Monitoring and correction of the stress in an anchor bolt based on pulse pre-pumped Brillouin optical time domain analysis," *Energy Science & Engineering*, vol. 8, no. 6, pp. 2011–2023, 2020.
- [32] L. Li, S. Sun, J. Wang, W. Yang, S. Song, and Z. Fang, "Experimental study of the precursor information of the water inrush in shield tunnels due to the proximity of a water-filled cave," *International Journal of Rock Mechanics and Mining Sciences*, vol. 130, Article ID 104320, 2020.
- [33] L. Jiang, Y. Zhao, N. Golsanami, L. Chen, and W. Yan, "A novel type of neural networks for feature engineering of geological data: case studies of coal and gas hydrate-bearing sediments," *Geoscience Frontiers*, 2020, in Press.
- [34] N. Golsanami, J. Sun, Y. Liu et al., "Distinguishing fractures from matrix pores based on the practical application of rock physics inversion and NMR data: a case study from an unconventional coal reservoir in China," *Journal of Natural Gas Science and Engineering*, vol. 65, pp. 145–167, 2019.